

# Plasmonic Dye-Sensitized Solar Cells

I-Kang Ding, Jia Zhu, Wenshan Cai, Soo-Jin Moon, Ning Cai, Peng Wang, Shaik M Zakeeruddin, Michael Grätzel, Mark L. Brongersma, Yi Cui,\* and Michael D. McGehee\*

Dye-sensitized solar cells (DSCs) have received wide-spread research attention due to their high power conversion efficiency and low cost.<sup>[1,2]</sup> Improving light harvesting in the 600 – 900 nm wavelength range, where state-of-the-art ruthenium-complex sensitizers absorb weakly, is one promising pathway to increasing power conversion efficiency to over 15%.<sup>[2]</sup> There have been multi-pronged research efforts to increase the light absorption of DSCs by developing strong absorbing dyes and using energy relay dyes.<sup>[3–5]</sup> Here, we report for the first time the use of plasmonic effects<sup>[6,7]</sup> to increase the light absorption and efficiency of DSCs. Plasmonic back reflectors, which consist of 2D arrays of silver nanodomes, were incorporated into solid-state dye-sensitized solar cells (ss-DSCs) by nanoimprint lithography. The reflectors enhance absorption through excitation of plasmonic modes and increased light scattering. ss-DSCs with plasmonic back reflectors show increased external quantum efficiency, particularly in the long wavelength region of the dye's absorption band. Consequently, ss-DSCs made with ruthenium-complex sensitizers (Z907) and strong-absorbing organic sensitizers (C220) have 16% and 12% higher short-circuit photocurrents, respectively. They achieve power conversion efficiencies of 3.9% and 5.9%, on par with the world record for devices with the same dyes.

SS-DSCs use solid-state hole-transport materials (HTM) to replace conventional liquid electrolytes and offer a viable pathway towards higher efficiency because the open-circuit voltage can be tuned by adjusting the highest-occupied molecular orbital (HOMO) of the HTM.<sup>[8,9]</sup> The use of solid-state materials also solves the potential leakage problems associated with the volatility and corrosiveness of liquid electrolytes. An ss-DSC is composed of a mesoporous TiO<sub>2</sub> photoanode, which is sensitized with a monolayer of dye, filled with HTM, and capped by reflective metal contacts deposited on top of the active layer. Currently,

optimized ss-DSCs are still limited by electron–hole recombination<sup>[10]</sup> and incomplete pore filling of the HTM,<sup>[11,12]</sup> such that the optimized active layer is only 2 μm thick, much less than the thickness needed to achieve sufficient light absorption. Efforts to increase light absorption in ss-DSCs have primarily been focused on developing strong absorbing dyes<sup>[9]</sup> and new TiO<sub>2</sub> nanostructures with high internal surface area for dye adsorption;<sup>[13]</sup> few studies have attempted to optimize the optical properties of the structure of the ss-DSCs to enable better photon management.

The use of plasmonic effects has been proposed as a promising pathway to increase light absorption in active layers of solar cells,<sup>[6]</sup> and has been demonstrated on several thin-film solar-cell materials such as amorphous silicon,<sup>[14–16]</sup> gallium arsenide,<sup>[17]</sup> polymers,<sup>[18,19]</sup> and dye monolayers on TiO<sub>2</sub>.<sup>[20–22]</sup> Most of the reported plasmonic solar cells have substantially lower efficiency than state-of-the-art devices made with the same material, because the active layers used are significantly thinner than they normally are in cells. Studies on such thin cells have been of great value as they have unequivocally demonstrated that spectral enhancements in the photocurrent density can be obtained through: 1) excitation of localized surface plasmon resonances of metallic nanoparticles;<sup>[23]</sup> 2) scattering of light by metallic nanoparticles into dielectric-like waveguide modes of the solar cell;<sup>[24]</sup> and 3) coupling to propagating surface plasmon polariton (SPP) modes.<sup>[25]</sup> An important distinction is made here between the excitation localized surface plasmon (SP) resonances that occur when conduction electrons in finite-sized particles are driven into oscillation, and SPPs which are surface electromagnetic waves that propagate along metal surfaces. The efficient excitation of localized SP resonances depends on the geometry, size, shape, and dielectric environment of the metal particles and field enhancements are only produced in very close proximity to the metals (~10 nm). The propagating SPP waves can most efficiently be excited by generating periodic grating structures that allow free space light waves to pick up sufficient in-plane momentum to couple to the shorter wavelength (higher propagation constant) SPP waves.

Whereas SPPs have their highest field intensity at the metal/dielectric interface, they also exhibit a large penetration depth (100 nm – 1 μm) into the dielectric medium adjacent to the metal.<sup>[26]</sup> For this reason, the excitation of SPP can produce absorption enhancements in thicker active layers in a solar cell. It should also be mentioned that coupling to dielectric waveguide modes can be enhanced by exploiting plasmonic effects; near the surface plasmon frequency of metallic particles, their scattering ability (i.e. cross section) is resonantly enhanced and the scattering into both dielectric-like and SPP modes can be increased.

Here, we demonstrate for the first time that both the SPP- and scattering-induced effects as mentioned above can be

I.-K. Ding, Dr. J. Zhu, Dr. W. Cai, Prof. M. L. Brongersma, Prof. Y. Cui, Prof. M. D. McGehee  
Department of Materials Science and Engineering  
Stanford University  
Stanford, CA 94305, USA  
Email: yicui@stanford.edu; mmcgehee@stanford.edu  
Dr. S.-J. Moon, Dr. S. M. Zakeeruddin, Prof. M. Grätzel  
Institut de Chimie Physique  
École Polytechnique Fédérale de Lausanne  
1015 Lausanne, Switzerland  
N. Cai, Prof. P. Wang  
State Key Laboratory of Polymer Physics and Chemistry  
Changchun Institute of Applied Chemistry  
Chinese Academy of Sciences  
Changchun 130022, P.R. China

DOI: 10.1002/aenm.201000041

utilized to enhance the light absorption and efficiency of a highly optimized, not optically thin, solar cell through the use of a plasmonic back reflector that features a 2D array of nanoscale metallic domes. This approach leads to power conversion efficiencies on par with the world record reported for these cells.

Key to the realization of a useful plasmonic back reflector is the identification of an inexpensive fabrication procedure that can produce a plasmonic structure of the right size, shape, and spacing. The height variations required to turn the top electrode into an effective plasmonic back reflector were incorporated into the TiO<sub>2</sub> mesoporous active layer of ss-DSCs using nanoimprint lithography (NIL). The direct imprinting process allows for a one-step pattern transfer from a master to the TiO<sub>2</sub> active layer, which eliminates the need for additional post-processing steps, such as pattern transfer from a NIL resist to the active layer. To the best of our knowledge, this is the first report of using NIL to pattern mesoporous TiO<sub>2</sub> films. In the imprinting process, a hexagonally close-packed nanodome pattern with periodicity around 900 nm and peak-to-valley height around 400 nm was first fabricated in a quartz master by Langmuir-Blodgett assembly of silica nanoparticles, followed by reactive ion-etching<sup>[27]</sup> (Figure 1b). Then, the master template was embossed into a film containing

TiO<sub>2</sub> nanoparticles and ethyl cellulose. After the NIL patterning process, the TiO<sub>2</sub> film subsequently underwent standard ss-DSC fabrication procedures:<sup>[28]</sup> sintering at 450 °C (Figure 1c), TiCl<sub>4</sub> treatment, dye sensitization, spiro-OMeTAD (2,2',7,7'-tetrakis-(*N,N*-di-*p*-methoxyphenylamine)-9,9'-spirobifluorene) infiltration, and thermal evaporation of a silver electrode. As seen in the cross-sectional scanning electron microscopy (SEM) image of the final device (Figure 1d), the nanodome pattern on the TiO<sub>2</sub> film was maintained in both the spiro-OMeTAD overlayer and the metal electrode layer with high fidelity.

In order to elucidate how the plasmonic back reflector enhances absorption, we performed three-dimensional full-wave electromagnetic simulations using the finite-element method. The schematic of the device architecture is shown in Figure 2a, with structural parameters extracted from the SEM image in Figure 1d, including the center-to-center distance of 900 nm, the nanodome base radius of 300 nm, and the nanodome height of 200 nm. In the numerical study we first assumed that the metallic nanostructure is covered with a uniform, non-absorbing dielectric, which helps to reveal the optical characteristics of the device and the plasmonic properties of the hexagonal array of silver nanodomains in particular. Figure 2a also shows slice plots of the magnetic field intensity of the cell, as normalized by the incident field magnitude (See Figure 2a). The illumination wavelength for this plot was chosen to be 600 nm, within the absorption band of the dyes. The magnetic field magnitude was plotted as it most naturally visualizes the excitation surface plasmon polaritons, which produce surface currents and associated strong magnetic fields near the metal surface. The field plots show many maxima and minima in the field intensity, which are characteristic for a structure that is many wavelengths thick and supports a large number of optical modes. High fields that decay away from the metal surface are also observed on and near the metal dome and these are characteristic of plasmonic excitations.

In order to assess whether the dome structure can produce an absorption enhancement over a planar metallic mirror, we show the spectral dependence of the energy density enhancement in the ss-DSC active layer (Figure 2b). The plot shows a number of peaks spread out over the considered wavelength range. In an ultrathin, plasmon-enhanced solar cell the number of such peaks is typically limited to two or three and they can easily be associated with the excitation of localized SP resonances and well-defined waveguide modes. For the thick solar cell considered here, many peaks are expected, some overlapping, because the structure supports a great number of waveguide modes in addition to localized particle resonances. As the nanodome array exhibits multiple length scales both within the dome structure

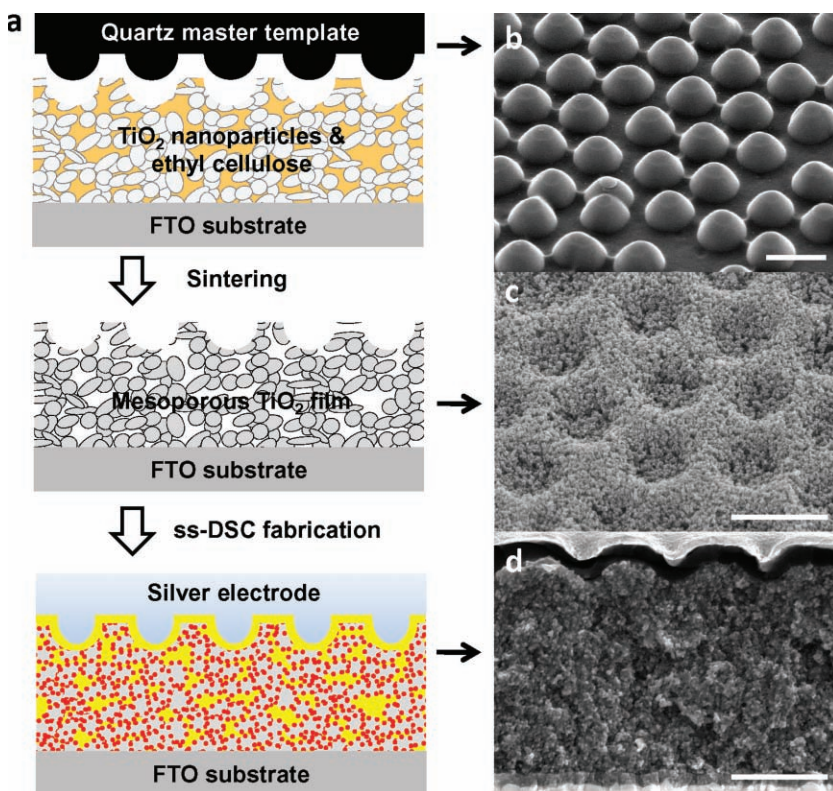


**Figure 1.** Schematic illustration of plasmonic ss-DSC fabrication process and the scanning electron microscopy (SEM) images of the nanodome array and plasmonic ss-DSC. a) Schematic of the plasmonic ss-DSC fabrication process. The sintering step is carried out in air to remove the ethyl cellulose from the TiO<sub>2</sub> film. The ss-DSC fabrication procedures include the following steps: TiO<sub>2</sub> film is treated with TiCl<sub>4</sub> aqueous solution, sensitized with dye molecules (red dots), infiltrated with spiro-OMeTAD (yellow), and silver electrode is evaporated on top. b) 45°-tilt SEM image of the nanodome quartz template. c) 45°-tilt SEM image of imprinted mesoporous TiO<sub>2</sub> film after sintering. d) cross-sectional SEM image of plasmonic ss-DSC, with 2D array of silver nanodomains in the back contact. Scale bars in (b–d): 1 μm.

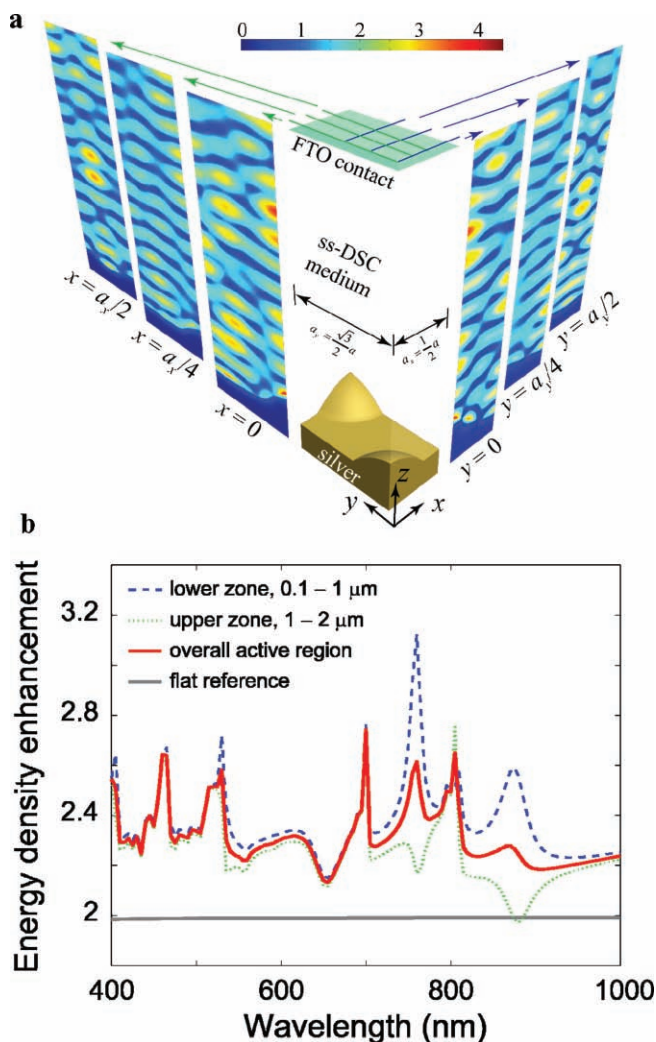


**Figure 2.** Plasmonic back reflector with nanodome arrays leads to an enhanced concentration of the electromagnetic energy in ss-DSCs as compared to a reference cell with a flat back reflector. a) A quarter of the equivalent rectangular unit cell of the hexagonal array with a lattice constant  $a = 900$  nm. Slice plots show the magnitude of normalized magnetic field at a number of representative locations for a representative illumination wavelength of 600 nm. b) Energy density enhancement in the ss-DSC as a function of the wavelength. The solid red line represents the normalized energy density in the entire active region of 2  $\mu\text{m}$  in height, excluding the 100 nm overlayer immediately above the silver surface. The dashed and dotted curves show the same quantity in close proximity of the nanopattern (within 1  $\mu\text{m}$  from the silver structure, spiro-OMeTAD overlayer excluded) and in the upper zone of 1–2  $\mu\text{m}$  from the silver, respectively. The solid gray line represents the enhancement in the reference cell with a flat silver reflector.

and the array, coupling to many of the allowed modes is possible. Rather than pursuing a strict modal decomposition of the enhancement, in these thick structures it makes more sense to have a pragmatic separation between plasmonics and dielectric waveguiding effects. For this reason, we hypothetically split the 2- $\mu\text{m}$ -thick dielectric region into a lower zone (spiro-OMeTAD overlayer excluded) of 0.1–1  $\mu\text{m}$  away from the metal surface in which both SPPs and light scattering contribute substantially

to the energy buildup, and an upper zone where SPPs contribute very little to the overall absorption. Although seemingly complex, Figure 2b reveals a number of spectral features associated with the hexagonal array of silver nanodomains and the mechanisms that help to boost the solar cell efficiency. For example, the resonances at wavelengths of 760 nm and 870 nm favoring only the energy buildup in the lower zone represent excited standing waves of SPPs in the flat metallic surfaces and around the domes, respectively. In contrast, the relatively sharp peaks at about 700 nm and 805 nm correspond to the coupling of scattered light into multimodal guided waves in the dielectric region, which is reasonably uniform across the entire 2  $\mu\text{m}$  slab. We note that in actual devices, the resonant behavior would be less pronounced than that shown in Figure 2b, owing to both the non-uniformity of geometrical parameters (dome height, shape, and spacing) and the absorption-induced damping in the solar cell. For comparison, we include in the same plot the energy density enhancement in a previously optimized reference cell where a flat silver back-reflector is used. In this reference case the enhancement factor possesses an almost constant value of slightly less than 2. Within the wavelength range of interest, the overall energy density in the nanodome-based structure is increased by about 20% as compared to the flat reference. When a realistic absorptive medium is used in the dielectric region, an improved light-harvesting capability is expected in nanodome-based plasmonic ss-DSCs, as the light absorption in the active region is directly related to the magnitude of the electric field squared (i.e. the light intensity).

SS-DSC devices that incorporate plasmonic back reflectors were tested under simulated 100  $\text{mW cm}^{-2}$  AM1.5G illumination. SS-DSCs with planar, non-imprinted  $\text{TiO}_2$  film and planar silver electrodes were used as control devices. Two sensitizing dyes were used in this study. Z907 is a ruthenium-complex sensitizer commonly used for ss-DSCs that has a peak extinction coefficient of 12,200  $\text{M}^{-1} \text{cm}^{-1}$  at 525 nm and a weak absorption tail that extends up to 750 nm.<sup>[29]</sup> C220 is a metal-free organic sensitizer with a very high peak extinction coefficient of 62,700  $\text{M}^{-1} \text{cm}^{-1}$  at 525 nm and an absorption tail that drops off sharply above 600 nm.<sup>[30]</sup> Since the main advantage of using plasmonic back reflectors is to enhance absorption, the potential efficiency improvement should be higher for Z907 since it does not absorb as strongly. The current density-voltage ( $J$ - $V$ ) characteristics of the ss-DSC devices are shown in Figure 3a,b and key device parameters are listed in Table 1. For devices made with Z907 dye (Figure 3a), the plasmonic nanostructure increased the short-circuit photocurrent ( $J_{\text{SC}}$ ) by 16%, and the power conversion efficiency (PCE) increased from 3.15% for control devices to 3.87%. For devices made with C220 dye (Figure 3b), the  $J_{\text{SC}}$  increased by 12% and PCE increased from 5.64% to 5.93%. In addition to the photocurrent enhancement, the nanoimprinted devices also show a higher fill factor, which might be a consequence of the nanoimprinted pattern reducing the effective distance the electrons and holes have to travel to reach the electrodes, resulting in better charge collection. Whereas the open-circuit voltage ( $V_{\text{OC}}$ ) remained relatively unchanged for Z907-based devices, it decreased noticeably for C220-based devices. The discrepancy in the extent of  $V_{\text{OC}}$  decrease is outside the scope of this study, but it may be due to the difference in recombination

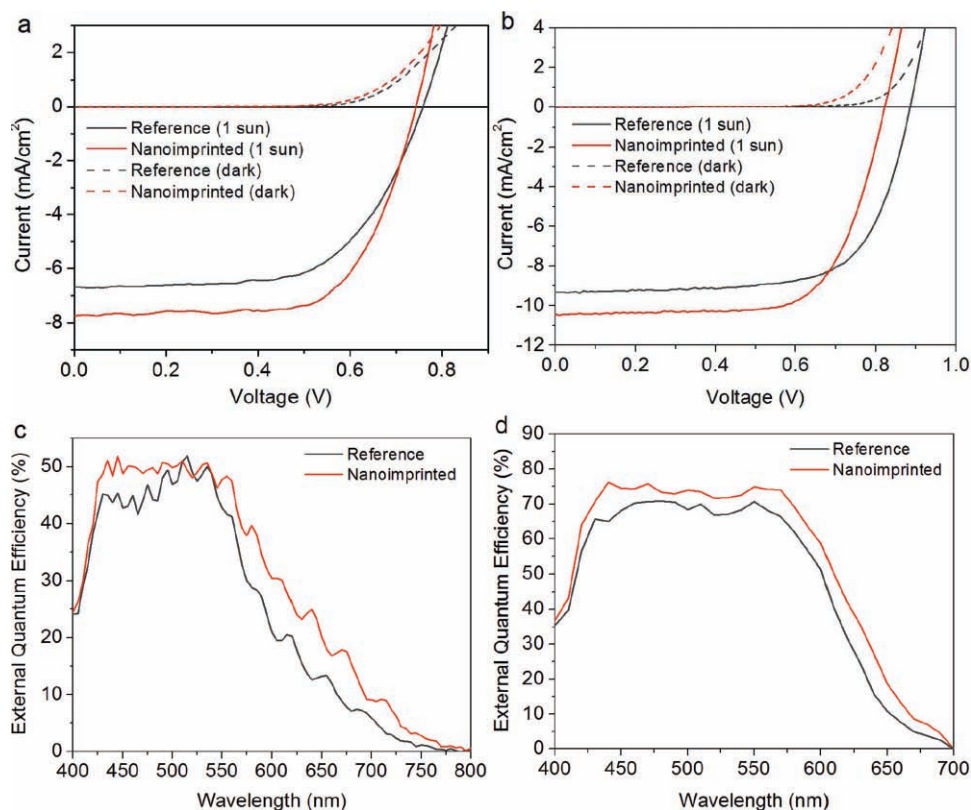


**Figure 3.** Photovoltaic characterization of ss-DSCs with plasmonic nanostructure. a,b) Current density – voltage ( $J$ - $V$ ) curves of ss-DSCs made with Z907 dye (a) and C220 dye (b). Solid lines represent the  $J$ - $V$  curves of nanoimprinted devices (red) and control devices (black) acquired under AM 1.5G ( $100 \text{ mW/cm}^2$ ) illumination. Dashed lines represent the  $J$ - $V$  curves of the same set of devices, acquired in the dark. c,d) External quantum efficiency (EQE) spectra of ss-DSCs made with Z907 dye (c) and C220 dye (d). The EQE curves were taken with chopped monochromatic illumination in conjunction with a continuous  $10 \text{ mW/cm}^2$  white light bias.

kinetics between the organic dyes and ruthenium-complex dyes.<sup>[31]</sup>

To scrutinize the origin of the  $J_{\text{SC}}$  increase, we measured the external quantum efficiency (EQE) spectra (Figure 3c,d). An EQE measurement is more relevant than an absorption measurement on solar cells for determining enhancement in dye absorption because it can decouple the light absorption in the active layer from the parasitic absorption caused by the nanostructured silver electrodes. For the Z907-device (Figure 3c), the EQE increases over the whole wavelength range, and the enhancement is more pronounced between 550–750 nm where the Z907 dye does not absorb strongly. For the C220-device (Figure 3d), the EQE enhancement is lower because C220 has a higher extinction coefficient and a sharper drop-off in the

**Table 1.** Solar cell parameters of ss-DSC devices based on two different dyes.

	$J_{\text{sc}}$ [ $\text{mA/cm}^2$ ]	$V_{\text{oc}}$ [V]	Fill Factor	Efficiency [%]
Reference (Z907)	6.69	0.755	0.62	3.15
Nanopatterned (Z907)	7.74	0.745	0.67	3.87
Reference (C220)	9.32	0.885	0.68	5.64
Nanopatterned (C220)	10.44	0.822	0.69	5.93

absorption tail. Nonetheless, the increase in the EQE indicates that even for strongly-absorbing organic dyes, the patterned metal can still enhance absorption and increase  $J_{\text{SC}}$ .

Based on our simulations, the absorption enhancement can be attributed to the excitation of surface plasmon polariton (SPP) modes and the light scattering from metallic nanodomains. As shown in the optical simulation, SPP modes can enhance the absorption in the spatial region within a dielectric decay length of SPPs ( $\sim 1 \mu\text{m}$ ) from the silver electrode. Since the field strength of SPP modes decays exponentially with the distance from the electrode, we expect the plasmonic enhancement of photocurrent to increase when the spiro-OMeTAD overlayer thickness is decreased. Experimentally, we indeed found that the  $J_{\text{SC}}$  enhancement was influenced by the thickness of spiro-OMeTAD overlayer. The device shown in Figure 3a has a spiro-OMeTAD overlayer thickness around 150 nm, with  $J_{\text{SC}}$  enhancement around 16% from the reference. When the spiro-OMeTAD overlayer thickness is increased to 200 nm, the silver

nanodome size remains unaltered, but the  $J_{\text{SC}}$  enhancement drops to 10%. This observation confirms the contribution of SPP modes to the photocurrent, as the scattering-induced enhancement in the absorption is known to be less sensitive to the thickness of the inactive overlayer.

In conclusion, we have developed a one-step direct imprinting process for incorporating plasmonic silver nanodome arrays in the back reflectors of ss-DSCs. The imprinting process is inexpensive and scalable, and allows precise control over the feature size and periodicity. The resulting nanodome array greatly enhances the light absorption of ss-DSCs through light scattering and coupling to propagating surface plasmon polariton modes. The short-circuit photocurrent ( $J_{\text{sc}}$ ) is enhanced by 16% for ss-DSCs made with Z907 dye and by 12% for ss-DSCs made with C220 dye. The increase in photocurrent results from an EQE enhancement over a broad wavelength range, which is consistent with simulations.

This approach is complementary to the development of new dyes, and our results show that even cells with strong-absorbing organic dyes can benefit from the plasmonic nanodome array. Such design of plasmonic back reflectors that consist of sub-wavelength size metallic structures is not limited to dye-sensitized solar cells; it can potentially be applied to any thin-film solar cell materials

systems with active layer thickness on the scale of 0.5–10  $\mu\text{m}$ , such as amorphous silicon,<sup>[15,16,27]</sup> CdTe and Cu(In,Ga)Se<sub>2</sub>.

## Experimental Section

**Nanoimprinting TiO<sub>2</sub> Mesoporous Films:** FTO substrates (Apollo-FTO-HVT, ITRI, 1.1-mm thick) were cleaned and then coated with a compact layer of TiO<sub>2</sub> (50 nm) by aerosol spray pyrolysis using air as the carrier gas, following procedures published elsewhere.<sup>[28]</sup> TiO<sub>2</sub> nanoparticle paste was prepared by diluting commercially available paste (Dyesol 18NR-T) with terpineol (Fluka). The paste was deposited onto the FTO substrate by doctor-blading, which was performed inside a lamellar flow hood to avoid particle contamination. After doctor-blading, the FTO substrate was heated to 125 °C for 10 min in air to remove the solvents in the paste, leaving TiO<sub>2</sub> nanoparticles and ethyl cellulose in the film. The quartz master used in the nanoimprinting process was fabricated by Langmuir-Blodgett assembly of close-packed monodisperse SiO<sub>2</sub> nanoparticles followed by reactive ion-etching,<sup>[27]</sup> and was subsequently modified with self-assembled monolayer of tridecafluoro-1,1,2,2-tetrahydrooctyltrichlorosilane as a releasing agent.<sup>[32]</sup> Then, the TiO<sub>2</sub> film was imprinted with the quartz master at 180 °C under a pressure of 70 bars for 1 min using a commercial nanoimprinting machine (Obducat). The nanoimprinting process did not further compact the TiO<sub>2</sub> film because the ethyl cellulose occupied the spaces between TiO<sub>2</sub> nanoparticles. Consequently, the porosity and the surface area of the mesoporous TiO<sub>2</sub> film remained unaltered.

**Dye Sensitization:** After nanoimprinting, the mesoporous TiO<sub>2</sub> films were sintered at 450 °C in air. The resulting mesoporous TiO<sub>2</sub> films were 2.0–2.2  $\mu\text{m}$  thick. The device fabrication was completed following procedures published elsewhere.<sup>[28]</sup> For Z907-ssDSCs, the TiO<sub>2</sub> film was immersed in 0.3 mm Z907 dye solution (Solaronix SA) in 1:1 mixture of acetonitrile and tert-butyl alcohol for 12–18 h. The synthesis and characterization of C220 dye is reported elsewhere.<sup>[30]</sup> For C220-ssDSCs, the TiO<sub>2</sub> film was immersed in 0.1 mm C220 dye solution in 1:1 mixture of acetonitrile and tert-butyl alcohol for 2 h. After dye sensitization, the spiro-OMeTAD solution was spun coated onto the device.

**Spiro-OMeTAD infiltration:** Spiro-OMeTAD (EMD Chemicals; Merck GmbH) was dissolved in chlorobenzene in concentration of 225 mg/mL. 4-tertbutyl pyridine (tbp) was added to the solution with a volume to mass ratio of 1:10.3  $\mu\text{L}/\text{mg}$ . Lithium bis(trifluoromethylsulfonyl) imide salt (Li-TFSI) ionic dopant was pre-dissolved in acetonitrile at 170 mg/mL, then added to the HTM solution at 1:4.8  $\mu\text{L}/\text{mg}$  of Li-TFSI solution:spiro-OMeTAD. Upon changing the concentration of spiro-OMeTAD in the solution, the ratio of spiro-OMeTAD to tbp and Li-TFSI was kept constant. In the spiro-OMeTAD infiltration process, a small quantity (30  $\mu\text{L}$ ) of the spiro-OMeTAD solution was deposited onto each TiO<sub>2</sub> film and spun-coated at 2000 RPM for 45 s in air. After spin-coating, the film was stored inside a desiccator for 4 h prior to electrode evaporation.

We note that during plasmonic ss-DSC fabrication process, the thickness of the spiro-OMeTAD overlayer must be carefully controlled. If the overlayer is too thin (<100 nm), the silver electrode may come in direct contact with TiO<sub>2</sub> and result in shunting pathways; if the overlayer is too thick (>300 nm), the spiro-OMeTAD will fill in the nanodome pattern in TiO<sub>2</sub> and planarize the silver electrode. The optimum spiro-OMeTAD overlayer thickness is around 100 – 200 nm and can be tuned by adjusting the solution concentration between 180 – 225 mg/mL.

**Back Contact and Photovoltaic Measurements:** For efficiency measurements, silver electrodes (200 nm) were thermally evaporated onto the film under vacuum below 10<sup>-6</sup> Torr. Current density-voltage (*J*-*V*) measurements were carried out using procedures published elsewhere.<sup>[11,28]</sup> The external quantum efficiency (EQE) measurement was taken at short circuit using monochromated white light from a 100 W tungsten lamp (Newport), which was focused through a SpectraPro 150

monochromator (Acton Research). The monochromated illumination, chopped at 40 Hz, was superimposed on top of a continuous-wave white light illumination (10% sun) incident on the device. The photocurrent action spectrum of the device was acquired through a lock-in amplifier (SR830, Stanford Research Systems), and EQE was calculated by comparing the photocurrent action spectrum of the device to that of a NIST traceable calibration photodiode.

**Optical Simulations:** The 3D full-wave numerical study is carried out using a commercial numerical package COMSOL Multiphysics. In our simulations, the permittivity of silver is taken from accepted experimental data,<sup>[33]</sup> and an effective index of 1.8 is assumed for the dielectric region, in accordance with published data.<sup>[34]</sup> Due to the symmetric nature of the hexagonal structure, only a quarter of the equivalent rectangular unit cell containing two quarter-domes is needed in the computations, with appropriate periodic conditions applied to all lateral boundaries and perfect matched layers along the light propagating direction. In actual devices, the resonant behavior would be less pronounced than that shown in Figure 2b, owing to both the non-uniformity of geometrical parameters (dome height, shape, and spacing) and the absorption-induced damping in the solar cell. Nonetheless, the overall enhancement in the light absorption is expected to be about 20% over the reference cell, as indicated by the spectrally averaged improvement in the energy density.

## Acknowledgements

I.-K. D. and J. Z. contributed equally to this work. This publication was partially based on work supported by the Center for Advanced Molecular Photovoltaics (Award No KUS-C1-015-21), made by King Abdullah University of Science and Technology (KAUST). Y.C. acknowledges the partial support from U.S. Department of Energy under the Award Number DE-FG36-08GO18004. W.C. and M.L.B. also wish to acknowledge Department of Energy for partial support of this work. N.C. and P.W. are grateful to the National Key Scientific Program (No. 2007CB936700) and the National Science Foundation of China (No. 50973105) for financial support. We thank Professor Shan X. Wang, Dr. Chris M. Earhart and Mingliang Zhang for assistance with nanoimprint lithography, Eric T. Hoke for assistance with external quantum efficiency measurements, and Professor Henry J. Snaith for helpful discussions.

Received: October 28, 2010

Revised: November 28, 2010

Published online: December 14, 2010

- [1] B. C. O'Regan, M. Grätzel, *Nature* **1991**, 353, 737.
- [2] M. Grätzel, *Acc. Chem. Res.* **2009**, 42, 1788.
- [3] C. Y. Chen, M. Wang, J. Y. Li, N. Pootrakulchote, L. Alibabaei, N.-L. Cevy-Ha, J. D. Decoppet, J. H. Tsai, C. Grätzel, C. G. Wu, S. M. Zakeeruddin, M. Grätzel, *ACS Nano* **2009**, 3, 3103.
- [4] B. E. Hardin, E. T. Hoke, P. B. Armstrong, J.-H. Yum, P. Comte, T. Torres, J. M. J. Frechet, M. K. Nazeeruddin, M. Grätzel, M. D. McGehee, *Nat. Photon.* **2009**, 3, 406.
- [5] J.-H. Yum, B. E. Hardin, S.-J. Moon, E. Baranoff, F. Nüesch, M. D. McGehee, M. Grätzel, M. K. Nazeeruddin, *Angew. Chem. Int. Ed.* **2009**, 48, 9277.
- [6] H. A. Atwater, A. Polman, *Nat. Mater.* **2010**, 9, 205.
- [7] J. A. Schuller, E. S. Barnard, W. Cai, Y. C. Jun, J. S. White, M. L. Brongersma, *Nat. Mater.* **2010**, 9, 193.
- [8] U. Bach, D. Lupo, P. Comte, J. E. Moser, F. Weissortel, J. Salbeck, H. Spreitzer, M. Grätzel, *Nature* **1998**, 395, 583.
- [9] J.-H. Yum, P. Chen, M. Grätzel, M. K. Nazeeruddin, *ChemSusChem* **2008**, 1, 699.
- [10] F. Fabregat-Santiago, J. Bisquert, L. Cevy, P. Chen, M. Wang, S. M. Zakeeruddin, M. Grätzel, *J. Am. Chem. Soc.* **2009**, 131, 558.

- [11] I.-K. Ding, N. Tetreault, J. Brillat, B. E. Hardin, E. H. Smith, S. J. Rosenthal, F. Sauvage, M. Gratzel, M. D. McGehee, *Adv. Funct. Mater.* **2009**, *19*, 2431.
- [12] H. J. Snaith, R. Humphry-Baker, P. Chen, I. Cesar, S. M. Zakeeruddin, M. Grätzel, *Nanotechnology* **2008**, *19*, 424003.
- [13] E. J. W. Crossland, M. Kamperman, M. Nedelcu, C. Ducati, U. Wiesner, D. M. Smilgies, G. E. S. Toombes, M. A. Hillmyer, S. Ludwigs, U. Steiner, H. J. Snaith, *Nano Lett.* **2008**, *9*, 2807.
- [14] D. Derkacs, S. H. Lim, P. Matheu, W. Mar, E. T. Yu, *Appl. Phys. Lett.* **2006**, *89*, 093103.
- [15] V. E. Ferry, M. A. Verschuuren, H. B. T. Li, R. E. I. Schropp, H. A. Atwater, A. Polman, *Appl. Phys. Lett.* **2009**, *95*, 183503.
- [16] V. E. Ferry, M. A. Verschuuren, H. B. T. Li, E. Verhagen, R. J. Walters, R. E. I. Schropp, H. A. Atwater, A. Polman, *Opt. Express* **2010**, *18*, A237.
- [17] K. Nakayama, K. Tanabe, H. A. Atwater, *Appl. Phys. Lett.* **2008**, *93*, 121904.
- [18] A. J. Morfa, K. L. Rowlen, T. H. Reilly, M. J. Romero, J. v. d. Lagemaat, *Appl. Phys. Lett.* **2008**, *92*, 013504.
- [19] K. Tvingstedt, N.-K. Persson, O. Inganäs, A. Rahachou, I. V. Zozoulenko, *Appl. Phys. Lett.* **2007**, *91*, 113514.
- [20] C. Häggglund, M. Zäch, B. Kasemo, *Appl. Phys. Lett.* **2008**, *92*, 013113.
- [21] S. D. Standridge, G. C. Schatz, J. T. Hupp, *J. Am. Chem. Soc.* **2009**, *131*, 8407.
- [22] C. Wen, K. Ishikawa, M. Kishima, K. Yamada, *Sol. Energy Mater. Sol. Cells* **2000**, *61*, 339.
- [23] B. P. Rand, P. Peumans, S. R. Forrest, *J. Appl. Phys.* **2004**, *96*, 7519.
- [24] R. A. Pala, J. S. White, E. S. Barnard, J. Liu, M. L. Brongersma, *Adv. Mater.* **2009**, *21*, 3504.
- [25] V. E. Ferry, L. A. Sweatlock, D. Pacifici, H. A. Atwater, *Nano Lett.* **2008**, *8*, 4391.
- [26] W. L. Barnes, *J. Opt. A: Pure Appl. Opt.* **2006**, *8*, S87.
- [27] J. Zhu, C.-M. Hsu, Z. Yu, S. Fan, Y. Cui, *Nano Lett.* **2010**, *10*, 1979.
- [28] I.-K. Ding, J. Melas-Kyriazi, N.-L. Cevy-Ha, K. G. Chittibabu, S. M. Zakeeruddin, M. Grätzel, M. D. McGehee, *Organic Electronics* **2010**, *11*, 1217.
- [29] M. K. Nazeeruddin, S. M. Zakeeruddin, J. J. Lagref, P. Liska, P. Comte, C. Barolo, G. Viscardi, K. Schenk, M. Graetzel, *Coord. Chem. Rev.* **2004**, *248*, 1317.
- [30] R. Li, J. Liu, N. Cai, M. Zhang, P. Wang, *J. Phys. Chem. B* **2010**, *114*, 4461.
- [31] B. O'Regan, I. Lopez-Duarte, M. V. Martinez-Diaz, A. Forneli, J. Albero, A. Morandeira, E. Palomares, T. Torres, J. R. Durrant, *J. Am. Chem. Soc.* **2008**, *130*, 2906.
- [32] W. Hu, R. J. Wilson, L. Xu, S.-J. Han, S. X. Wang, *J. Vac. Sci. Technol., A* **2007**, *25*, 1294.
- [33] P. B. Johnson, R. W. Christy, *Phys. Rev. B* **1972**, *6*, 4370.
- [34] A. J. Moule, H. J. Snaith, M. Kaiser, H. Klesper, D. M. Huang, M. Gratzel, K. Meerholz, *J. Appl. Phys.* **2009**, *106*, 073111.